

**GT2025-151174**

## EXPERIMENTAL INVESTIGATION OF ENHANCED HEAT SINKS FOR HYBRID ELECTRIC AIRCRAFT

**Faezeh Rasimarzabadi**  
 National Research Council Canada  
 Ottawa, Ontario, Canada

**Utkarsh Sheel Anand**  
 Carleton University  
 Ottawa, Ontario, Canada

**Evgueni Bordatchev**  
 National Research Council Canada  
 London, Ontario, Canada

**Hassan Azarkish**  
 Calogy Solutions  
 Sherbrooke, Quebec, Canada

**Mahmood Shirazy**  
 Calogy Solutions  
 Sherbrooke, Quebec, Canada

### ABSTRACT

Controlling the temperature of onboard battery systems is a key thermal management challenge for hybrid electric aircrafts. Initially, a standard plate-fin heat sink was used in an innovative approach to dissipate heat generated by battery cells in electric vehicles. However, based on an analysis of a kW-scale hybrid electric aircraft, two heat sinks were specifically optimized for the aircraft's application: pin-fin and micro-structured heat sinks. This paper compares the performance of these optimized heat sinks with that of the original plate-fin heat sink.

A custom-designed box was created to direct airflow into the heat sinks, modeled in accordance with the specifications used in CFD analysis. Testing was conducted across two different airflow rate ranges. The results showed that the optimized heat sinks outperform the original in terms of thermal performance and weight. Experimental results indicated a more substantial performance enhancement with the pin-fin heat sink than what the simulations predicted. Significant improvements were observed using optimized pin-fin heat sink at higher airflow rates and greater source powers. At lower airflow rates, the micro-structured heat sink, produced through advanced micromachining, proved to be the optimal choice, delivering the best performance with the lightest weight.

Keywords: heat transfer, hybrid electric aircraft, heat sink, battery

### NOMENCLATURE

$A$	Surface area (m <sup>2</sup> )
$C_p$	Specific heat capacity (W/kg K)
$H$	Height (m)
$L$	Length (m)
$m$	Mass flow rate (kg/s)

$P$	Power (W)
$P$	Pressure (Pa)
$Q$	Heat transfer rate (W)
$T$	Temperature (°C, K)
$V$	Velocity (m/s)
$W$	Width (m)
$X$	Distance (m)
$X_k, Y_k, Z_k$	Kinematic motions (m)
$X_s, Y_s$	Scanning motions (m)
CFD	Computational Fluid Dynamics
CFM	Cubic Foot per Minute
DAS	Data Acquisition System
EDM	Electrical Discharge Machining
EXP	Experimental
HEAT	Hybrid Electric Aircraft Testbed
HS	Heat Sink
HTC	Heat Transfer Coefficient

### 1. INTRODUCTION

Effective thermal management is critical for the performance and reliability of high-power density electronic devices. Pin-fin heat sinks are popular for cooling applications due to their superior heat transfer capabilities [1]. However, designing these heat sinks involves balancing thermal performance, pressure drop, and manufacturing constraints. A novel hybrid heat sink design that integrates microchannels and stepped pin-fins effectively managed hotspots in microprocessors [2]. The key findings of this study were improved heat temperature uniformity, enhanced heat transfer and targeted hotspot management. Topology optimization techniques have emerged as powerful tools for designing high performance heat sinks. Pin-fin heat sinks were optimized with

variable fin density under natural convection, demonstrating improved thermal performance [3]. A genetic algorithm coupled with the CFD was used to optimize both the profile and pattern of pins in a pin-fin heat sink [4]. The optimized designs showed 15-20% better thermal performance and lower pressure drop than conventional in-line pin arrangements. Rectangular pins perform better thermally than other shapes, while triangular pins perform the worst. This is attributed to the greater surface extension of thin rectangular pins and the lower density of triangular pins under the heat source.

Micro-structured heat sinks have emerged as a promising solution for high heat flux thermal management in electronic devices and other applications. By incorporating features such as microchannels, micro-pin-fins, and manifold designs at the microscale, these heat sinks can significantly enhance convective heat transfer and overall thermal performance compared to conventional heat sink designs. A comprehensive thermal performance analysis of micro-pin-fin heat sinks was conducted by Nunes, et al. [5] showing that taller micro-pins provide lower thermal resistance which is of interest. It was highlighted that optimizing the flow conditions can lead to a 25-30% improvement in the overall thermal performance of micro-pin-fin heat sinks, making them highly effective for cooling high-power electronic devices. The impact of gradually expanding flow passages on the flow boiling characteristics of micro-pin-fin heat sinks was studied by Markal, et al. [6]. The decreasing pin-fin density in the flow direction suppressed flow instabilities and reduced pressure drop compared to the uniformly distributed pins. The effect of surface microstructures created by various surface engineering methods was studied on the heat dissipation performance of heat sinks [7]. It was found that increasing surface roughness through microstructures enhanced thermal emissivity by up to 2.5 times and improved overall heat dissipation, especially when combined with a thermal radiation coating. A comprehensive review of recent advancements in microchannel flow designs was conducted by Zhang, et al., including sawtooth, serpentine, bionic fractal, wavy, double-layer, and manifold configurations [8]. These designs have been systematically analyzed to elucidate their effects on thermal performance and fluid flow characteristics. The study found that enhanced structures within microchannels, such as ribs and fins, significantly augment heat transfer by increasing turbulence and surface area. Additionally, the incorporation of porous media and cavities further enhances thermal conductivity and fluid mixing, leading to improved overall heat transfer efficiency. Other researchers have explored applying surface texturing and laser-etched microstructures to enhance heat transfer [9]. They demonstrated that fabricating temperature-selective thermal radiation surfaces through surface texturing can enable more precise temperature selectivity for emitted radiation from heat sinks. This approach has the potential to improve thermal management in electronic devices. The design of surface microstructures was optimized on high-efficiency heat dissipation fins [10]. The effects of microstructure thickness, geometry, and spacing were analyzed, finding that these parameters can significantly improve the

thermal performance of high-heat-flux electronic devices by enhancing thermal convection, radiation, and conduction.

Calogy Solutions, Ltd. (Sherbrooke, Quebec, Canada) has introduced an innovative approach for controlling battery cell temperatures in electric vehicles. Calogy's thermal management technology, called Uni.T, is a thin and highly thermally conductive sheet placed in contact with the cells within the battery pack to redistribute and transfer heat inside the pack efficiently by liquid-vapor phase change. However, their initial solution—a standard plate-fin heat sink—proved inefficient for aircraft applications [11]. This paper presents the design and testing of two optimized heat sinks specifically developed for the battery thermal management system of a kW-scale hybrid electric aircraft, and compares their performance with the original plate-fin heat sink. The optimization process included two key approaches: fin optimization and surface modification. Parametric studies were performed to identify optimal configurations, and multi-variable optimization using a weighted objective function was applied to select the best models. Optimization criteria included thermal and hydraulic performance, weight, and fabrication challenges, with each factor normalized and weighted based on its importance. More details about the two optimized heat sinks can be found in [11]. Testing of these models is detailed in this paper.

## 2. TEST SETUP AND INSTRUMENTATION

The fabricated models are shown in Figure 1. They are constructed from aluminum 6061. The original plate-fin heat sink, measuring 83.5 mm × 290.5 mm × 27 mm, features 24 fins. Each fin has a width of 1.1 mm, pitch of 2 mm and a height of 21 mm, as shown in Figure 1a. The optimized pin-fin heat sink (Figure 1b) features in-line square fins with a width of 1.1 mm, a height of 15 mm, and a pitch-to-height ratio of 0.15. The models were manufactured using Electrical Discharge Machining (EDM), a non-traditional process that removes material through repeated electrical discharges between electrodes and the workpiece, with a dielectric fluid present. Due to the size limitations of the available EDM machine, the heat sinks were produced in two separate pieces and then assembled by gluing. The glue joints between the halves of the heat sinks are aligned with the line of symmetry of the flow field and therefore, should not impact the thermal or flow performance. For the micro-structured heat sink (Figure 1c), the fins, which match the size and pitch of the original plate-fin heat sink, were manufactured separately and then attached to the base. This allowed for the surface modification with microstructures to be applied to both sides of each fin. The pattern featured staggered square microstructures with a height-to-width ratio of 4, considered a high aspect ratio. Afterward, the fins were stacked together and secured with screws. The aluminum rods, threaded at both ends, were fitted with nuts. Finally, the bottom face was machined flat after assembly. Efforts were made to ensure the laminated structure was as tight as possible to minimize heat spreading effects and contact resistance. To reduce the contact thermal resistance, the surfaces in contact were made as flat as possible to improve contact and minimize gaps where air could

accumulate, thus lowering thermal resistance. Additionally, higher pressure was applied at the interface to reduce the gap between surfaces and increase the contact area, enhancing heat transfer.

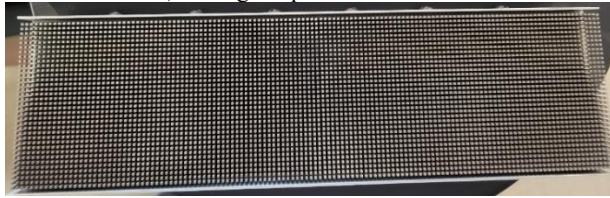
Table 1 compares the weights of the three heat sinks. The optimized pin-fin and micro-structured heat sinks are 20% and 27% lighter, respectively, compared to the original plate-fin heat sink.

**TABLE 1: WEIGHT OF THE HEAT SINKS**

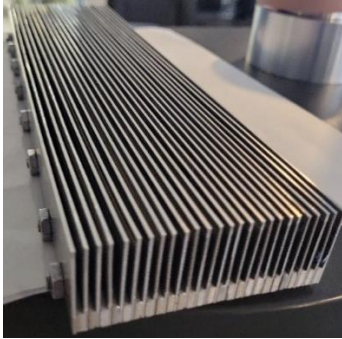
Type	Weight (kg)
Original plate-fin	0.82
Pin-fin	0.65
Micro-structured	0.63



a) Original plate-fin heat sink



b) Pin-fin heat sink



c) Micro-structured heat sink

**FIGURE 1: TESTED HEAT SINK MODELS**

For the test, a custom-designed box was created to direct airflow into the heat sink, modeled similarly to those used in CFD analysis [11]. As shown in Figure 2, the airflow comes from the top and passes through a duct and leaves the heat sink from two sides. The box shown in Figure 3, features a 3-D printed duct and a top surface. To ensure a proper seal around the heat sink, Neoprene foam was applied along the sides and underneath. Figure 4 shows a picture of the test setup. Testing was performed across two different airflow rate ranges. To achieve the higher range of flow rates, the inlet duct of the heat sink box was connected to a section downstream of the nozzle and wind tunnel flow conditioning area. The Pitot-static probe, positioned upstream of the duct, measures the total and static pressures as

well as the static temperature to estimate the air mass flow rate. The total pressure port of the Pitot-static probe is linked to a 15-psi absolute pressure sensor (accuracy:  $\pm 0.5\%$  of the full-scale range), while the pressure difference between the total and static ports is measured with a 10 inH<sub>2</sub>O differential pressure sensor, which has an accuracy of 0.025% of the full-scale range ( $\pm 0.6$  Pa). Inlet pressure at the heat sink is recorded using two static taps connected to 15-psi absolute pressure sensors. Outlet pressure is measured with four static taps connected to 10 inH<sub>2</sub>O differential pressure sensors, referenced with the total pressure port of the Pitot-static probe. A film heating element is mounted on the back of the heat sink and powered by an adjustable DC power supply. Voltage and current are measured with two calibrated multimeters. During testing, the power ranged from 25 W to 300 W. Air temperature at the two outlets is measured using immersion type-T thermocouples, assuming uniform temperature distribution and even flow across the outlet.

Eight type-T thermocouples (with an accuracy of  $\pm 0.5^\circ\text{C}$ ) are attached to the base of the heat sink, while two additional type-T thermocouples are placed between the film heating element and the heat sink. The Pitot-static probe uses a type-K thermocouple (with an accuracy of  $\pm 1^\circ\text{C}$ ) to measure the inlet air temperature. Data for pressure and temperature are collected using a NI CompaqRIO and data acquisition system (DAS).

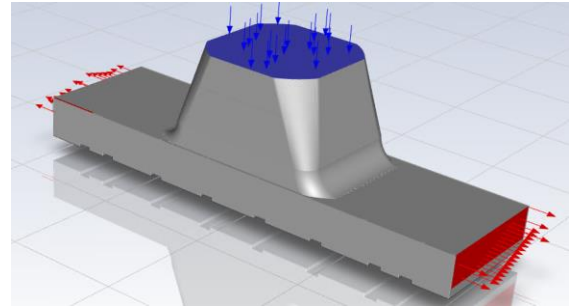


**FIGURE 2: CFD MODEL OF THE DUCT AND HEAT SINK**

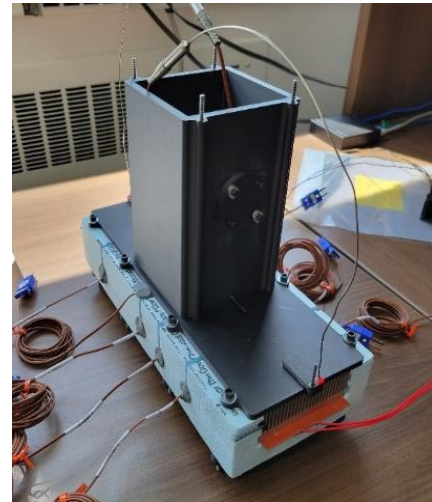


**FIGURE 3: HEAT SINK POSITIONED WITHIN THE FOAM AND BOX**



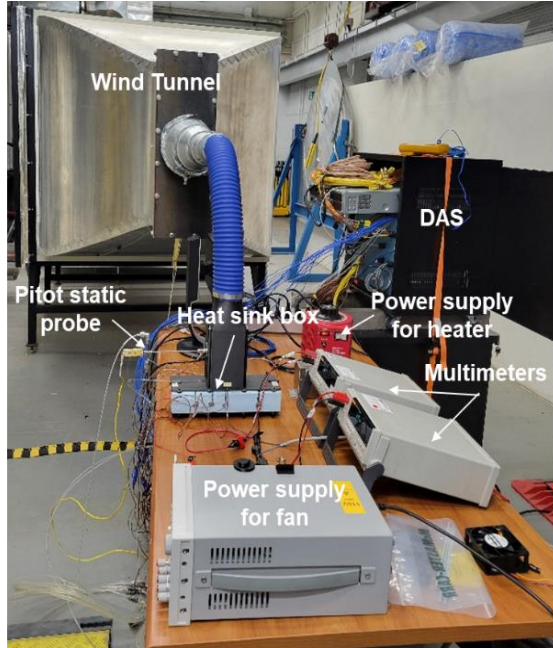


**FIGURE 4: TEST SETUP FOR HIGH AIRFLOW RATES**

### 3. FABRICATION OF THE MICRO-STRUCTURED HEAT SINK

Fabricating structures with high aspect ratios at micro- and nano-scales, often involves advanced microfabrication techniques, such as more developed and widely applied micromachining by laser ablation [12] and micromachining by material removal by cutting [13], and their combination [14].

#### 3.1 Laser Microfabrication System and Procedure

Laser texturing of flat fins was performed using a multi-axis opto-electro-mechanical laser processing system (Figure 5). The system uses a high-power pulsed fiber laser (IPG Photonics, USA, YLPN-2-20X500-200) with a wavelength of 1064 nm and a maximum power of 200 W. The laser emits pulses ranging from 20 ns to 500 ns in duration, with a repetition rate of 2 kHz to 4000 kHz. The laser beam, delivered through an optical fiber, passes through a collimator and camera unit, aligned with a galvanic optical mirror scanner. These mirrors are controlled by a computer numerically controlled (CNC) system, allowing the laser to move across the workpiece, focusing through an  $f$ -theta lens. The focal point on the fin's surface is adjusted using a CNC Z stage. The fin is mounted on a vise attached to an  $X$ - $Y$  CNC motion stage. This setup enables five motion axes, with three kinematic motions ( $X_k$ ,  $Y_k$ ,  $Z_k$ ) and two scanning motions ( $X_s$ ,  $Y_s$ ) via a galvanometric scanner (ScanLab GmbH, Germany) with a 100 mm  $\times$  100 mm working envelope.

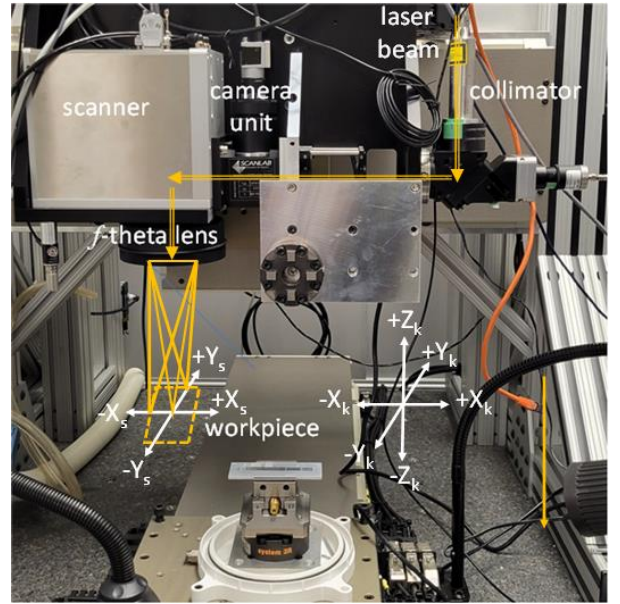


**FIGURE 5: LASER MICROFABRICATION SYSTEM**

Initial laser micromachining tests showed that the flat fin experienced thermodynamic deformation due to heat from the laser, causing significant bending (Figure 6) that affected the working distance and process performance.



**FIGURE 6: BENDING EFFECT AFTER LASER MICROFABRICATION**

To prevent such deformation, a holding fixture was designed (Figure 7). The fixture securely holds the fin, reducing the top portion to prevent bending while maintaining the structure's integrity. The fin was divided into 10 sub-areas of 20 mm  $\times$  27.2 mm to fit within the working envelope. Texturing was done by synchronizing the scanner and  $Y$ -axis motions. Each sub-area was scanned in 4 layers with 4 directional trajectories, achieving a height of 400–450  $\mu$ m. The process took 140 minutes per side, which can be optimized with better equipment.



**FIGURE 7: STRUCTURED FIN INSIDE THE HOLDING FIXTURE**

After structuring, re-deposited dust was found between pillars, except in the last sub-area. This dust can be removed using CO<sub>2</sub> or ultrasonic cleaning, but poses a potential health risk. Stitching junctions appeared between sub-areas due to material remelting at the start of each scan (Figure 8), which can be minimized with better control of laser power and motion

synchronization (Figure 9). These junctions slightly affect cooling media flow but do not significantly impact the final result.

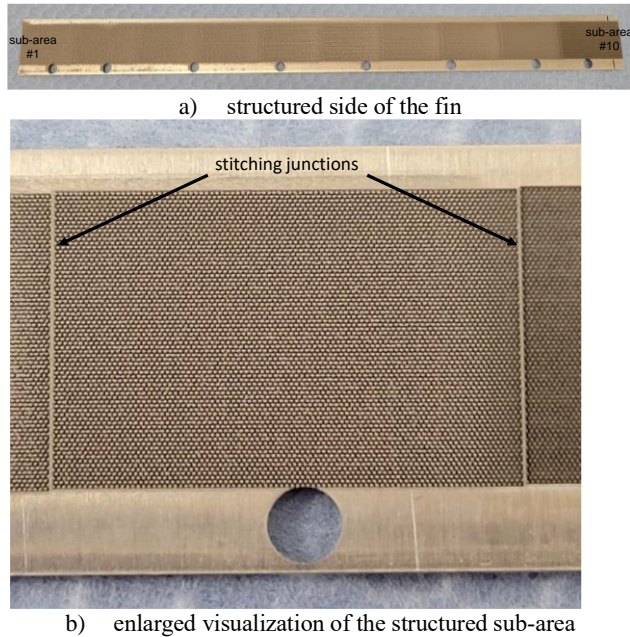


**FIGURE 8: EXAMPLE OF THE STRUCTURED FIN BEFORE CLEANING THE RE-DEPOSITED DUST**

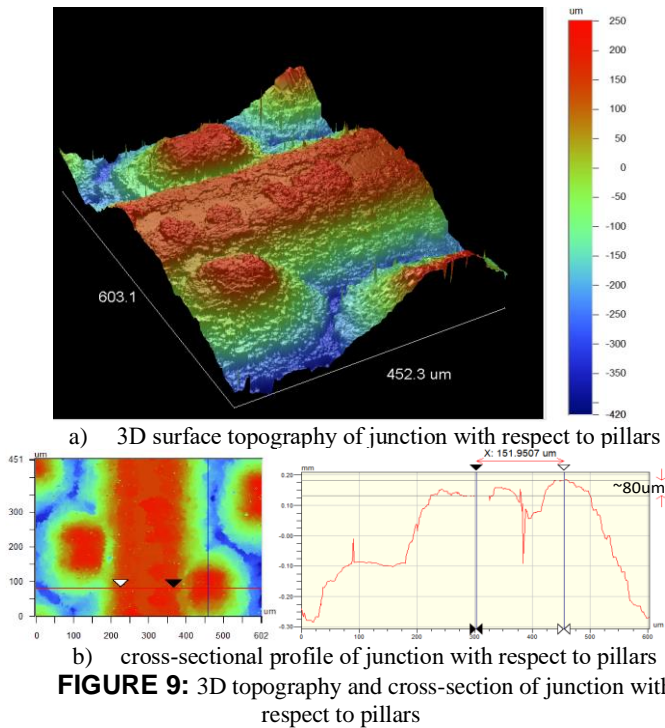


**FIGURE 9: 3D topography and cross-section of junction with respect to pillars**

### 3.2 Analysis of Machinability for Mass Production and Achieved Form Geometry

The proposed pillar design presents laser fabrication challenges due to its staggered configuration, unlike a standard

matrix layout. In a matrix setup, laser trajectories follow long straight grooves, maintaining constant process conditions. However, in the staggered design, pillars shift horizontally and vertically, blocking linear laser paths. This results in a combination of linear and non-linear movements, affecting the material removal rate and precision, leading to uncertain accuracy in the final structure.

To optimize processing speed and material removal rate, machinability tests were conducted at scanning speeds of 400 mm/s and 800 mm/s. For the 400 mm/s test, a 5 mm × 4 mm pocket was machined in 36 seconds, achieving a depth of 570 μm and a material removal rate of 0.317 mm<sup>3</sup>/s. At 800 mm/s, the same pocket was machined in 47 seconds, reaching a depth of 635 μm with a material removal rate of 0.270 mm<sup>3</sup>/s.

Further tests were performed to create high-aspect ratio structures, with speeds of 400 mm/s and 800 mm/s. At 400 mm/s, a height of 947 μm was achieved, demonstrating the ability to create structures with aspect ratios greater than 10. Increasing the speed to 800 mm/s resulted in a height of 753 μm, Figure 10. The 800 mm/s was chosen based on a compromise between processing speed, height of structures, and their form accuracy.

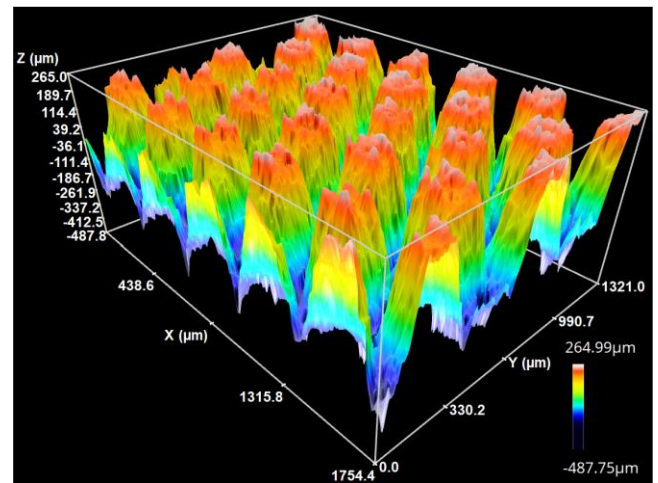
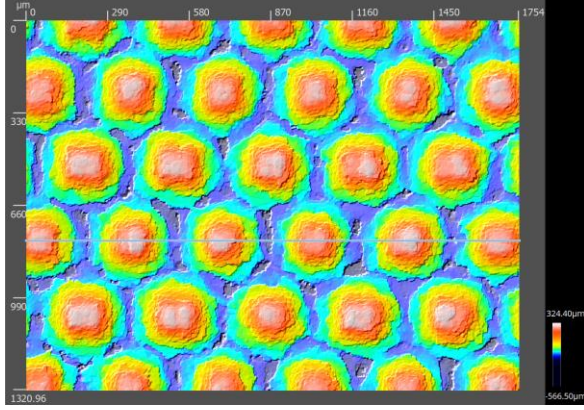


**FIGURE 10: MACHINABILITY ANALYSIS FOR 800 MM/S SCANNING SPEED**

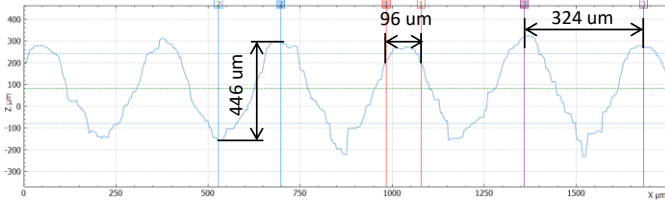
A balanced selection of process parameters, using 800 mm/s and 4 × 4 layers, was chosen for structuring the fins. The desired vertical square pyramid shape transformed into a column during structuring. Final results showed pillar heights ranging from 440 μm to 480 μm (target 400 μm), horizontal distances of 325 μm ± 5 μm (target 330 μm), and vertical distances of 530 μm ± 5 μm (target 530 μm), measured using a 3D optical profilometer, Figure 11.

These results provide valuable insights for future design, simulation, and fabrication of functional structures for various industrial applications.





a) 3D surface topography with a location of the measured horizontal cross-section



b) parameters of the horizontal cross-section

**FIGURE 11: EXAMPLE OF MEASURED FORM PARAMETERS FROM HORIZONTAL CROSS-SECTION**

#### 4. RESULTS AND DISCUSSION

The hydraulic and thermal performance of the optimized heat sinks is compared to the original plate-fin heat sink across different power levels, simulating heat generation from the battery cells. The thermal performance of the heat sinks is evaluated using the heat transfer coefficient ( $HTC$ ), calculated using Equation (1).

$$HTC = \frac{q}{A\Delta T} \quad (1)$$

Where,  $A$  represents the surface area of the heat sinks, which is  $0.343 \text{ m}^2$  for both the original and micro-structured heat sinks (assumed to be the same), and  $0.334 \text{ m}^2$  for the pin-fin heat sink. The temperature difference,  $\Delta T$ , is defined by Equation (2).

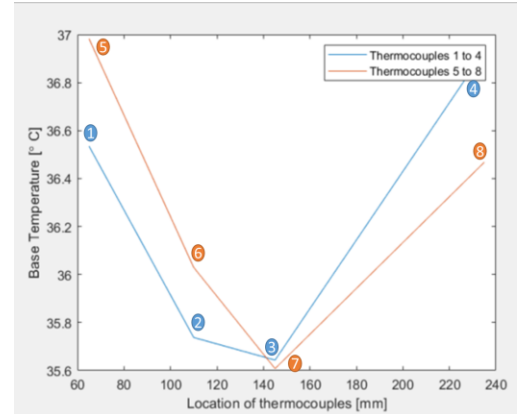
$$\Delta T = \frac{(T_{HS-in} - T_{in}) - (T_{HS-out} - T_{out})}{\ln\left(\frac{T_{HS-in} - T_{in}}{T_{HS-out} - T_{out}}\right)} \quad (2)$$

Figure 12 displays the locations of the base thermocouples, while Figure 13 presents a comparison of their data for two cases as an example. The temperature distributions follow a similar trend, with the lowest temperatures found at the center of the heat sink base. This is because air enters the heat sink at a lower temperature in the center, and as it moves through the heat sink toward the exits, it absorbs heat and its temperature increases. The heat sink temperature near the inlet, denoted as  $T_{HS-in}$  in Equation (2), is calculated as the average of readings from two thermocouples positioned at the center of the heat sink base (Thermocouples #3 and #7, as shown in Figures 12 and 13). The

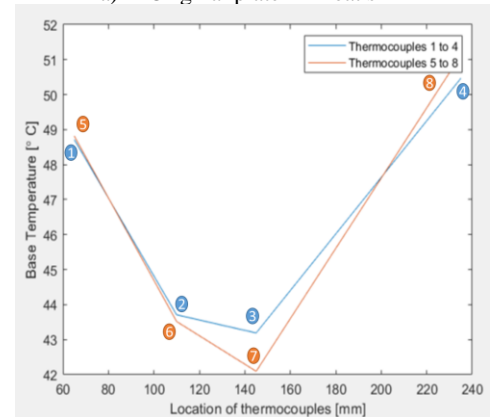
heat sink temperature near the outlet, denoted as  $T_{HS-out}$  is calculated as the average of the readings from the thermocouples: #1, #4, #5 and #8 (as shown in Figures 12 and 13).  $T_{in}$  represents the inlet air temperature, while  $T_{out}$  is the average air temperature at the two outlets.



**FIGURE 12: LOCATION OF THE BASE THERMOCOUPLES, X = 65 MM, 110 MM, 145 MM, 235 MM**



a) Original plate-fin heat sink



b) Pin-fin heat sink

**FIGURE 13: BASE TEMPERATURE DISTRIBUTION,  $P = 100 \text{ W}$**

A performance factor is defined in Equation (3) by comparing the ratios of heat transfer coefficients and pressure losses for the optimized heat sinks to those of the original plate-fin heat sink, which is denoted by the subscript "o".

$$\varepsilon = \frac{HTC/HTC_o}{\Delta P/\Delta P_o} \quad (3)$$

#### 4.1 Comparison of Heat Sink Performance at High Airflow Rates

For higher airflow rates (greater than approximately 30 CFM), a blower was employed, with the flow rate controlled by adjusting the blower frequency. Figure 14 presents a comparison of heat transfer coefficients ( $HTC$ ) at three power levels: 100 W, 200 W, and 300 W. The pin-fin heat sink, due to its high air resistance, results in lower airflow rates. In all cases, an increase in flow rate leads to a higher  $HTC$ . At 100 W, the  $HTC$  of the pin-fin heat sink is 59% higher than that of the original plate-fin heat sink, indicating a thermal enhancement. As power increases, the  $HTC$  of the pin-fin heat sink continues to improve, showing a 70.5% increase at 200 W and an 85.5% increase at 300 W. In contrast, the micro-structured heat sink does not show any improvement over the original plate-fin heat sink, except at the highest power level of 300 W, where it demonstrates a 13.5% increase in  $HTC$ . At lower flow rates, the thermal performance of the pin-fin heat sink appears to decrease significantly. To gain a better understanding, additional tests were conducted at these low airflow rates using a fan. The hydraulic performance is assessed by comparing the pressure drop across the heat sink, as illustrated in Figure 15. The average pressure drop for the pin-fin heat sink remains relatively consistent across all power levels, being approximately 400% to 450% higher than that of the original plate-fin heat sink, indicating an increase in air resistance. No significant difference is observed in the pressure drop between the original and micro-structured heat sinks. Note that for flow rates above approximately 40 CFM, the flow becomes turbulent. As a result, the microstructures have minimal impact on altering the fluid flow patterns, as well as the thermal and hydraulic performance. Figure 16 compares the performance factors of the heat sinks. Across all power levels and airflow rates, the micro-structured heat sink consistently outperforms the pin-fin heat sink, with  $\varepsilon > 1$ . This indicates that, when considering both thermal and hydraulic performance, the micro-structured heat sink is the optimal choice. However, if only thermal performance is considered and there are no constraints on providing high airflow rates, the pin-fin heat sink emerges as the better option.

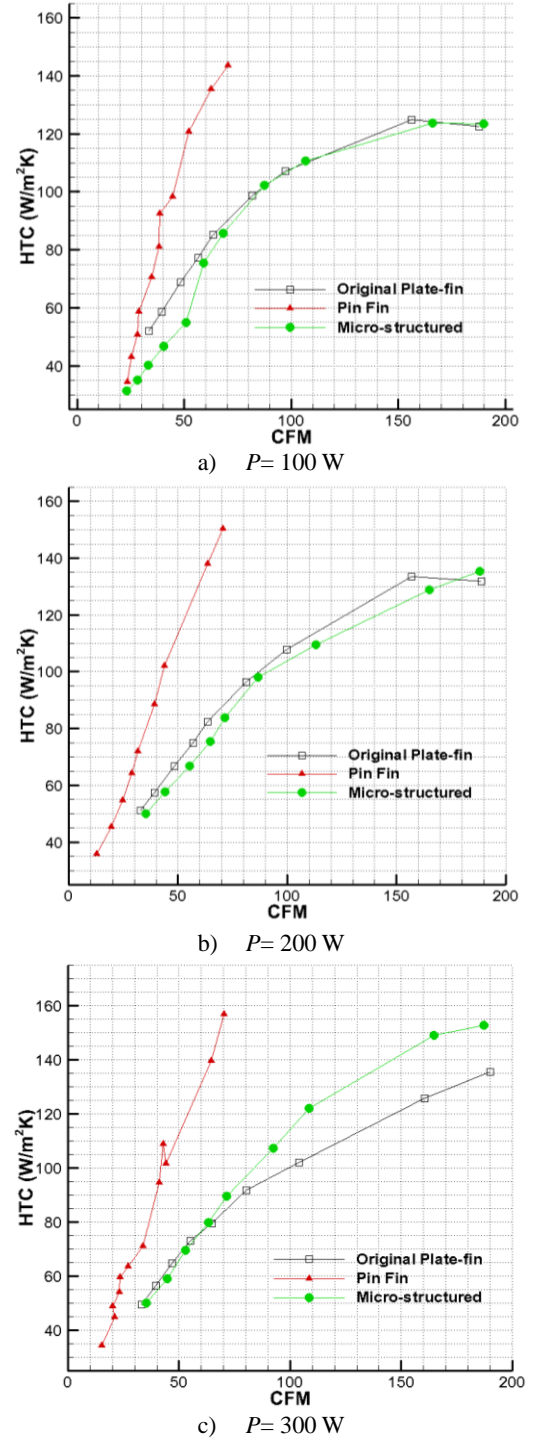
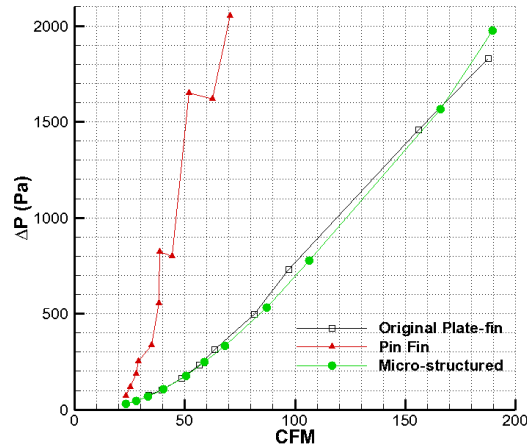
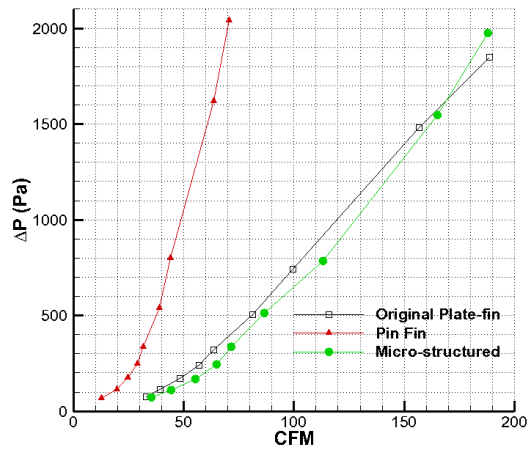


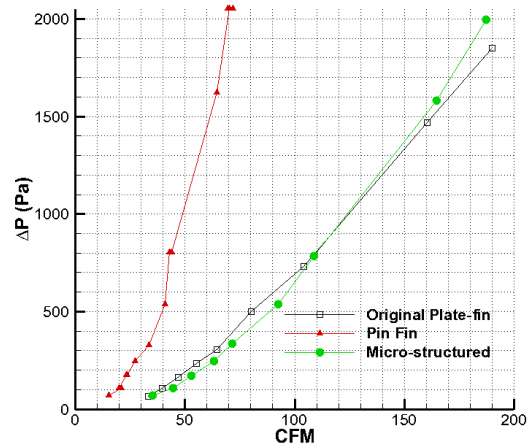
**FIGURE 14: HEAT TRANSFER COEFFICIENT AT DIFFERENT APPLIED POWERS**



a)  $P = 100 \text{ W}$



b)  $P = 200 \text{ W}$



c)  $P = 300 \text{ W}$

**FIGURE 15: PRESSURE DROP OVER THE HEAT SINK AT DIFFERENT APPLIED POWERS**

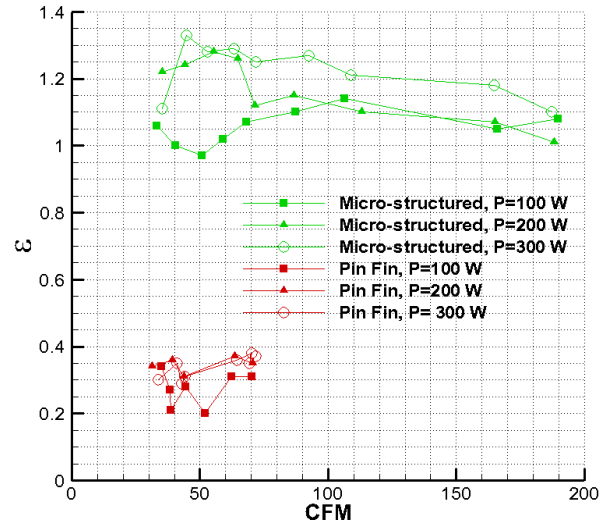


**FIGURE 16: PERFORMANCE FACTOR OF THE HEAT SINKS**

## 4.2 Comparison of Heat Sink Performance at Low Airflow Rates

To assess the performance of the heat sinks at lower flow rates, a fan was positioned at three different locations within the inlet duct, ranging from 5 mm to 35 mm above the top of the heat sink. Figure 17 and Figure 18 compare the thermal and hydraulic performance of the heat sinks at different power levels, with the fan set 5 mm from the heat sink. The power levels applied were 25 W, 50 W, and 100 W. Although the settings were identical for all heat sinks, the pin-fin heat sink exhibited lower flow rates due to its higher air resistance. Based on extrapolated data, the micro-structured heat sink demonstrated superior thermal performance compared to the other two heat sinks, consistent with results obtained using a blower at lower flow rates. The  $HTC$  for the micro-structured heat sink was approximately 23%, 26% and 28% higher than that of the original plate-fin heat sink as the source power increased. At this range of flow rates, where the flow is laminar, micro-structures can significantly alter the local surface area, fluid flow patterns, and heat transfer coefficients, resulting in complex changes in thermal performance. The pressure drop across the pin-fin heat sink was the highest, while the micro-structured heat sink exhibited a pressure drop similar to the original configuration. Figure 19 illustrates the effect of fan position on thermal performance of the heat sinks at a power level of 50W. The results show no significant advantage associated with the fan's placement.



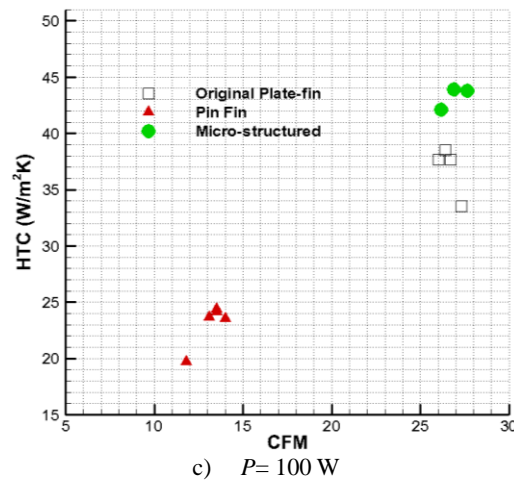
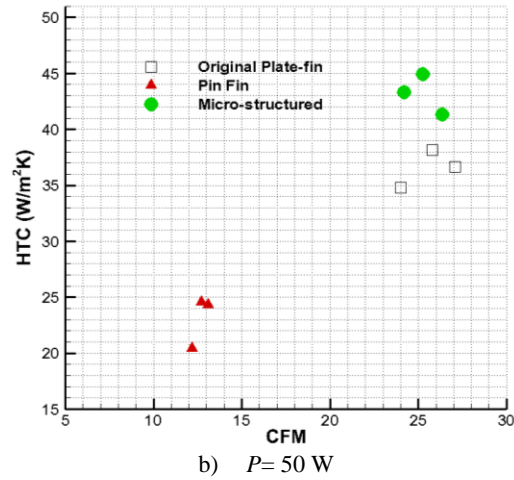
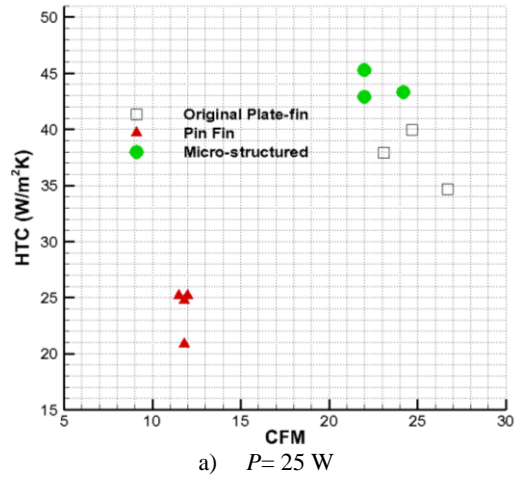


**FIGURE 17: COMPARISON OF THERMAL PERFORMANCE AT VARIOUS APPLIED POWER LEVELS WITH THE FAN POSITIONED 5 MM FROM THE HEAT SINK**

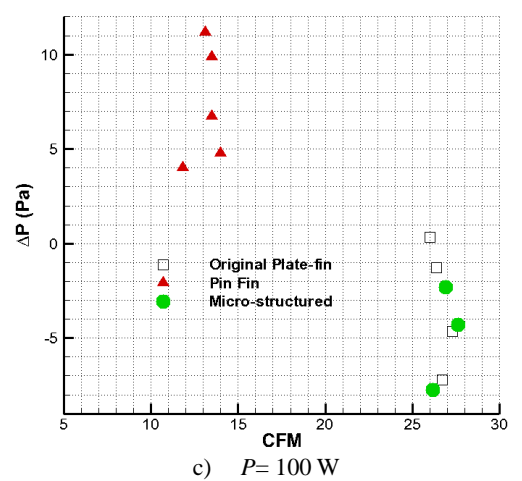
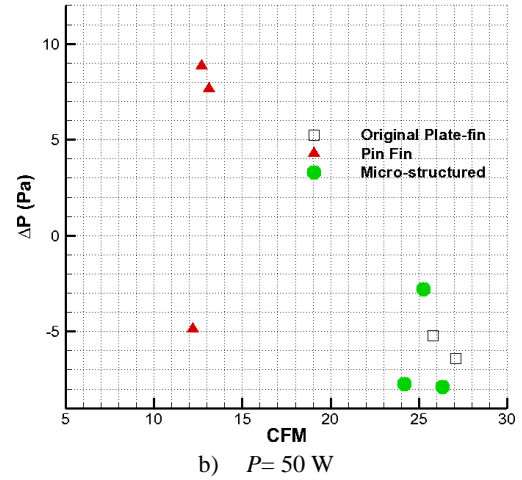
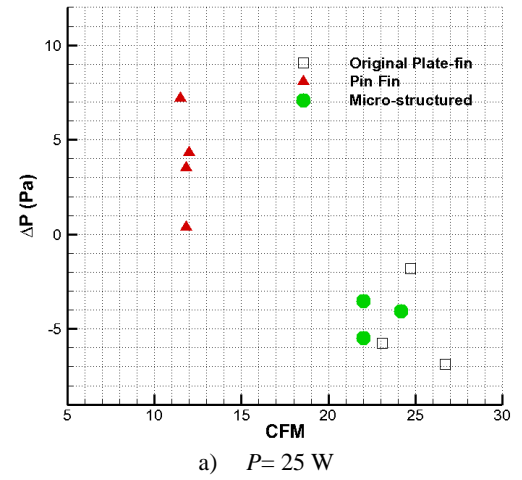


**FIGURE 18: COMPARISON OF HYDRAULIC PERFORMANCE AT VARIOUS APPLIED POWER LEVELS WITH THE FAN POSITIONED 5 MM FROM THE HEAT SINK**

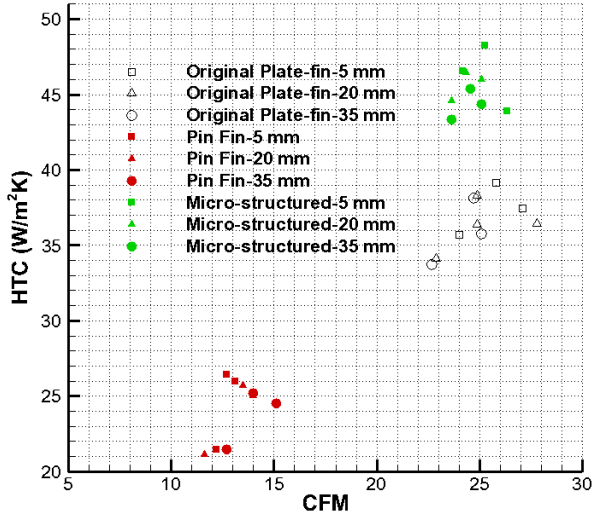


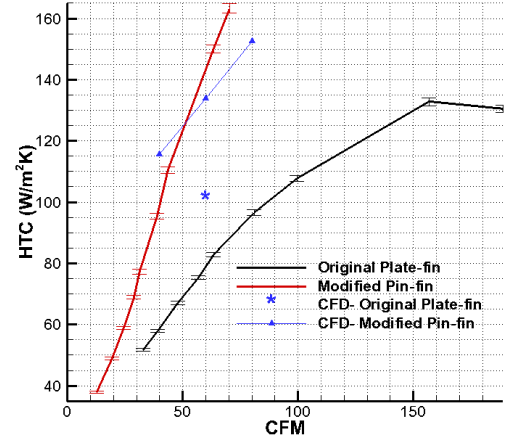
**FIGURE 19: IMPACT OF FAN POSITION ON THERMAL PERFORMANCE AT  $P=50W$**

## 5. COMPARISON THE RESULTS WITH THE CFD

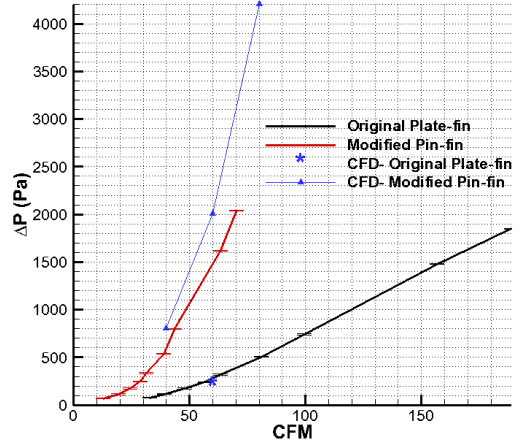
Figure 20 compares the experimental data with the numerical simulation results for a source power of 200 W. CFD data were available for one airflow rate of 60 CFM for the original plate-fin heat sink and for three airflow rates ranging from 40 CFM to 80 CFM for the pin-fin heat sink [15]. For the CFD analysis, the flow field was simulated using ANSYS FLUENT V2023 R2. A steady, pressure-based model was applied, with the Coupled solution method and Rhie-Chow flux type. The  $k-\omega$  SST turbulence model was selected, and a convergence criterion of  $10^{-6}$  was used for all variables. The solution domain was discretized using a Cartesian grid with unstructured hexahedral meshing. Further details can be found in [11] and [15].

The alignment between experimental and CFD results is reasonable for both the heat transfer coefficient and pressure drop. Overall, the experimental results suggest a greater improvement with the pin-fin heat sink compared to what is predicted by the numerical simulation. Table 2, compares the percentage difference between the pin-fin and original plate-fin heat sinks based on both numerical and experimental results at a flow rate of 60 CFM. The experimental results show a 70% improvement in the HTC, while the numerical results show a 33.4% improvement. The pressure difference in the experimental data indicates a 400% increase compared to the original heat sink, whereas the CFD results show a 979% increase. Discrepancies between experimental and CFD results can stem from several factors, including simplified assumptions in the CFD model, such as idealized boundary conditions, geometry, and turbulence models that may not accurately reflect real-world conditions. Differences in boundary conditions, flow rates, and geometry between the experiment and the CFD setup can also contribute. Measurement errors, environmental factors like temperature or pressure variations, and inaccuracies in fan or blower performance in experiments compared to CFD

assumptions can further affect the results. Additionally, numerical errors due to grid resolution or convergence issues in the CFD model may lead to discrepancies.



a) Heat transfer coefficient



b) Pressure drops

**FIGURE 20: COMPARISON OF THE RESULTS USING BLOWER WITH THE CFD,  $P=200W$**

**TABLE 2: COMPARISON OF NUMERICAL AND EXPERIMENTAL RESULTS**

Parameter	Differences between pin-fin and original plate-fin heat sinks	
	CFD	EXP
$HTC$ ( $W/m^2K$ )	33.4%	70%
$\Delta P$ (Pa)	979%	400%

Due to the high numerical cost, the CFD analysis of the micro-structures could not be performed on the full-scale heat sink model. Instead, it was conducted on a small section of the fin, with the results validated through experimental testing. The test setup is depicted in Figure 21. A duct with a bellmouth was designed, featuring a cross-sectional area of 20 mm  $\times$  2 mm. The fin samples have a length of 76.2 mm (3") and a width of 25.4 mm (1"). Made from brushed 6061 aluminum, each fin has a

thickness of 1.27 mm (0.0500"), as shown in Figure 21(a). One sample has a smooth surface, while the other features optimized microstructures. The test setup and duct assembly within the test section are illustrated in Figures 21(b) and 21(c). The velocity in the test section is controlled by adjusting the blower frequency using a Mitsubishi FR-PU04 Parameter Unit. The duct's entrance length is 200 mm, and an additional 50 mm length downstream of the fin is used for connecting the pressure tap and thermocouple at the outlet. Twelve Type-T thermocouples are glued to the base of the fin, while two heat flux sensors are positioned on the fin's back, between the fin and the film heating element, which is adhered to the fin. The duct assembly includes a bellmouth, a polycarbonate ceiling, and inlet and outlet sections. Neoprene foam is used in various locations to ensure proper sealing of the components and the duct. Pressure taps and thermocouples are glued into the polycarbonate ceiling, as shown in Figure 21(d).

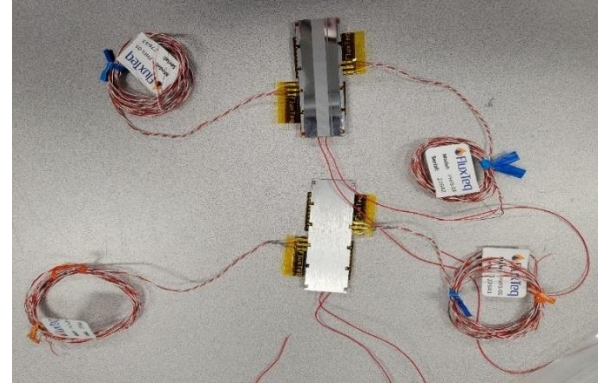
Figure 22 shows a cross-sectional view of the CFD domain. The numerical setup used was identical to the full-scale heat sink analysis, with the parameters summarized in Table 3. The mesh element size outside the duct was 1 mm, inside the duct was 0.1 mm, and on the fin, it was 0.05 mm. To align with the experimental conditions, the boundary conditions were set accordingly: air temperature at the inlet of the test section was 290.7 K, air velocity was 21.2 m/s, and the heat flux at the back of the fin was 710.4 W/m<sup>2</sup>, which corresponds to a heat source power of 1.08 W. Table 4 compares the CFD results with the experimental data for the micro-structured fin. The fin's surface area is 0.0035 m<sup>2</sup>. The discrepancy in the base temperature of the fin is minimal, with an error of only 0.01%. Overall, the numerical results show excellent agreement with the experimental data.

**TABLE 3: NUMERICAL SETUP PARAMETERS**

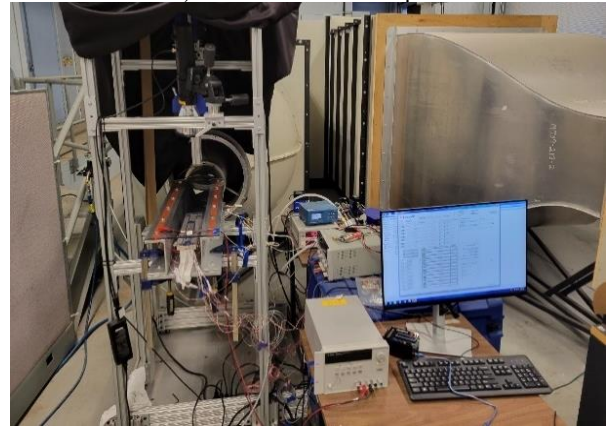
Parameter	Value
Mesh nodes	94 million
Element sizes	1 mm, 0.1 mm, 0.05 mm
Temperature inlet, $T_{in}$	290.7 K
Velocity inlet, $V_{in}$	21.2 m/s
Heat flux, $Q/A$	710.4 W/m <sup>2</sup>

**TABLE 4: COMPARISON THE NUMERICAL AND EXPERIMENTAL RESULTS FOR THE MICROSTRUCTURE FIN**

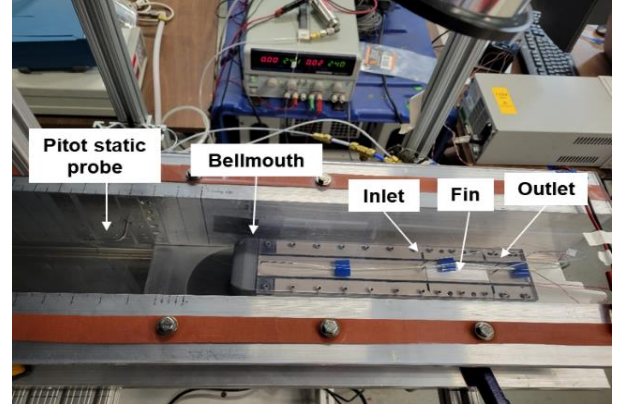
Parameter	CFD	EXP	% Discrepancy
Duct velocity, $V_{Duct}$ (m/s)	12.97	13.08	-0.84
Fin outlet temperature, $T_{out}$ (K)	292.61	291.94	0.23
Base temperature, $T_{Base}$ (K)	298.88	298.91	-0.01



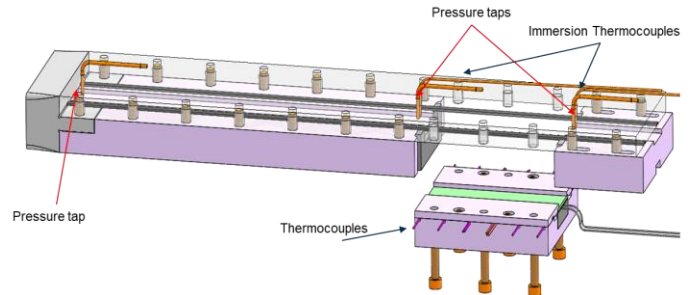
a) Two tested fin samples



b) A snapshot of the entire test setup



c) Duct in the test section



d) Measurement diagram on the duct

**FIGURE 21: TEST SETUP OF THE MICRO-STRUCTURED FIN TESTING**



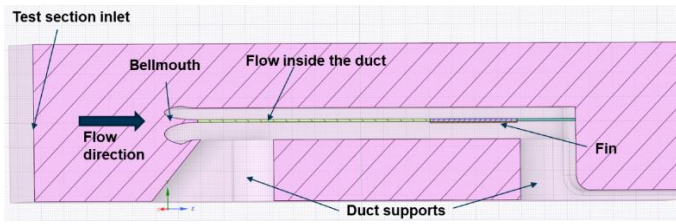


**FIGURE 22: CROSS VIEW OF THE CFD DOMAIN**

## 6. APPLICATION ON HEAT AIRCRAFT

The battery cell used in NRC's HEAT (Hybrid Electric Aircraft Testbed) aircraft was the SAMSUNG CS1200R. An aluminum plate has been used as a heat sink which is located under each battery module. In fact, there was a thermal interface material between the module and the aluminum plate. The battery pack contains a total of 192 cells in series. Assuming the average heat dissipation of the cruise phase is 25 W, then the total heat dissipation in this phase would be  $192 \times 25 \text{ W} = 4,800 \text{ W}$ . If each heat sink can remove 50 W, then 96 heat sinks are required for the battery pack ( $4,800 \text{ W} / 50 \text{ W} = 96$ ). It means each two-cells ( $192 / 96 = 2$ ) requires one Uni.T/heat sink combination. In this case, assuming the weight of each heat sink (the original plate-fin type) is 0.82 kg, the total weight of heat sinks will be 78.7 kg ( $96 \times 0.82 \text{ kg}$ ). Therefore, the weight of the heat sinks would be about 18% of the battery pack (422 kg). Using the optimized pin-fin and micro-structured heat sinks, the weight can be reduced by 20% and 27%, respectively. Furthermore, depending on the available airflow rate, using either of the pin-fin or micro-structured heat sink will result in increasing the heat transfer coefficient by the factor of about 70% and 26%, respectively.

A MATLAB code (using cells configuration and heat transfer equations) has been used to estimate the thermal capacity of the battery thermal management system. Figure 23 shows the plots of generated and dissipated heat and temperatures of six battery cells in 1.5 hours of flight simulation. In the left plots, the blue line is the rate of heat generation from six cells. The red line is the rate of heat dissipated from the aluminum plate or Uni.T/heat sink combination. The total generated heat is the integral under the blue line. The total dissipated heat is the integral under the red line. The ambient temperature during this flight is assumed to vary between 20°C and 0°C as indicated in green line of the right plots. From Figure 23(a), only 31.3% of the cells heat generation is transferred by the aluminum plate if the combination of Uni.T with the original plate-fin heat sink is not used. The cell temperature reaches more than 60°C after 1.5 hours of flight which is not acceptable as it exceeds the safe flight limit of 50°C. Using the combination of Uni.T with the original plate-fin heat sink, 83.4% of the heat generation of the cells is transferred by the heat sink as shown in Figure 23(b). Therefore, the cell temperature remains below 40°C. By 26% increase in the HTC using micro-structured heat

sink, 88% of the heat generation of the cells is transferred by the heat sink, as shown in Figure 23(c). The cell temperature remains below 35°C. It can be concluded that improving the heat sink thermal performance is highly effective in long term flights and can result in dissipating most of the cell heat generation to the ambient.

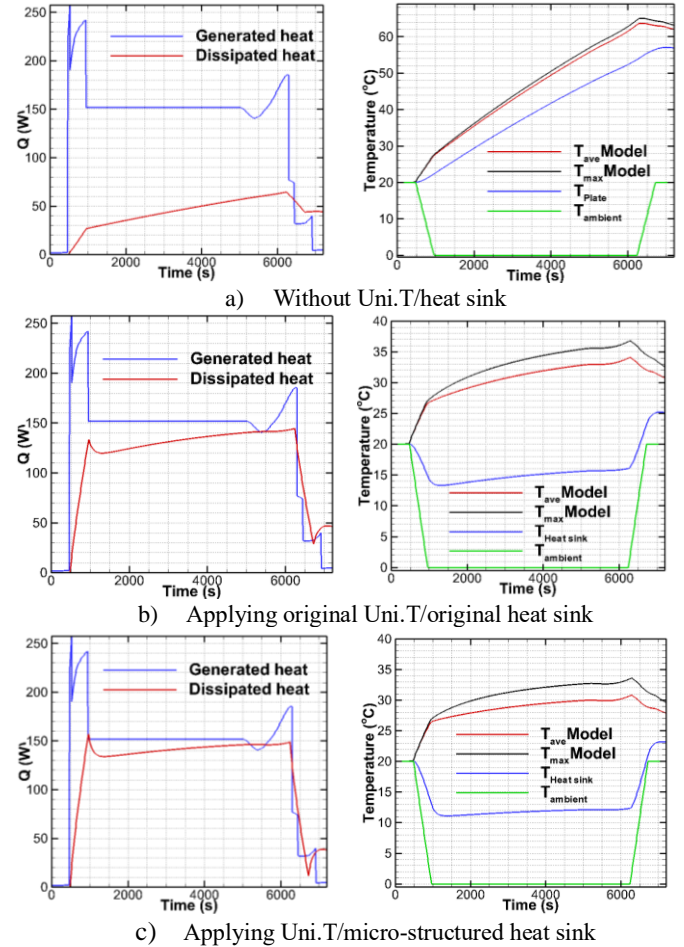


**FIGURE 23: RESULTS OF THE MODEL IN 1.5-HOUR FLIGHT**

## 7. CONCLUSION

The optimized pin-fin heat sink is the preferred choice for battery thermal management in a kW-scale hybrid-electric aircraft, provided that high airflow rates are available. It demonstrated up to an 85% increase in the heat transfer coefficient compared to the original heat sink. However, its hydraulic performance was lower than that of both the original plate-fin and micro-structured heat sinks. For lower airflow rates (below approximately 30 CFM), the micro-structured heat sink is the optimal option, offering the best performance while being 27% lighter than the original heat sink. The number of heat sinks needed for both types can be reduced by increasing the source power, which leads to additional weight savings.

## ACKNOWLEDGEMENTS

The authors would like to acknowledge the support of the NRC Low-Emissions Aviation Program and Calogy Solutions, Ltd. in this research.

## REFERENCES

- [1] N. Nisar Sheikh, B. Kumar, and N. Kumar Saini, "A Review Paper on Pin Fin Efficiency Enhancement," *International Journal of Applied Engineering Research*, ISSN 0973-4562 Vol. 14, No. 9, 2019.
- [2] D. Ansari, and K.Y. Kim, "Hotspot Management Using a Hybrid Heat Sink with Stepped Pin-Fins," *Numerical Heat Transfer, Part A: Applications*, Vol. 75, No. 6, 2019, pp. 359-380. DOI: 10.1080/10407782.2019.1599272
- [3] Y. J. Lee, and S. J. Kim, "Thermal Optimization of the Pin-Fin Heat Sink with Variable Fin Density Cooled by Natural Convection," *Applied Thermal Engineering*, Vol. 190, 116692, 2021. DOI: 10.1016/j.applthermaleng.2021.116692
- [4] W. Yang, Optimization of Pin Fin Heat Sinks for High Power Density Applications using Genetic Algorithms and CFD, *Master's Thesis*, University of Toronto, 2021.
- [5] J. M. Nunes, J. Diehl de Oliveira, J. B. Copetti, S. S. Gajghate, U. Banerjee, S. K. Mitra, and E. M. Cardoso, "Thermal Performance Analysis of Micro Pin-Fin Heat Sinks under Different Flow Conditions," *Energies*, Vol. 16, No. 3175, 2023. DOI: 10.3390/en16073175
- [6] B. Markal, B. Kul, M. Avci, and R. Varol, "Effect of Gradually Expanding Flow Passages on Flow Boiling of Micro Pin Fin Heat Sinks," *International Journal of Heat and Mass Transfer*, Vol. 197, No. 123355, 2022. DOI: 10.1016/j.ijheatmasstransfer.2022.123355
- [7] Y. You, B. Zhang, S. Tao, Z. Liang, B. Tang, R. Zhou and D. Yuan, "Effect of Surface Microstructure on the Heat Dissipation Performance of Heat Sinks used in Electronic Devices," *Micromachines*, Vol. 12, No. 265, 2021. DOI: 10.3390/mi12030265
- [8] X. Zhang, Z. Ji, J. Wang, and X. Lv, "Research Progress on Structural Optimization Design of Microchannel Heat Sinks Applied to Electronic Devices," *Applied Thermal Engineering*, Vol. 235, No. 121294, 2023. DOI: 10.1016/j.applthermaleng.2023.121294
- [9] C. Kuji, M. Ishii, R. Yoshikawa, M. Mizutani, and H. Soyama, "Fabrication of Temperature-Selective Thermal Radiation Surfaces Utilizing Surface Texturing," *Precision Engineering*, Vol. 82, 2023, pp. 1- 9
- [10] Y. Zhao, Y. Song, N. Zhuang, H. Zhao, and X. Tang, "Optimization Design of Surface Microstructure of High-Efficiency Space Radiation Heat Dissipation Fins," *Annals of Nuclear Energy*, Vol. 182, No. 109590, 2023. DOI: 10.1016/j.anucene.2022.109590
- [11] F. Rasimarzabadi, H. Azarkish, A. Crain, S. Recoskie, E. Bordatchev, and M. Shirazy, "Performance Improvement of a Heat Sink for Battery Thermal Management System," *ASME Journal of Engineering for Gas Turbines and Power*, Vol. 147, No. 3, 2025. DOI: 10.1115/1.4066703
- [12] K.E. Hazzan, M. Pacella, T.L. See, "Laser processing of hard and ultra-hard materials for micro-machining and surface engineering applications: A review," *Micromachines*, 12, paper 895, 2021. DOI: 10.3390/mi12080895
- [13] Z. Jiang, D. Chen, K. Sun, R. Pan, J. Fan, Y. Tang, "A systematic review of micro-texture formation based on milling: from mechanism, existing techniques, characterization to typical applications," *The International Journal of Advanced Manufacturing Technology*, 134, 2024, pp. 2151–2177, DOI: 10.1007/s00170-024-14177-4
- [14] A.K. Sahu, J. Malhotra, S. Jha, "Laser-based hybrid micromachining processes: A review," *Optics & Laser Technology*, 146, paper 107554, 2022. DOI: 10.1016/j.optlastec.2021.107554
- [15] F. Rasimarzabadi, and A. Crain, Heat Sink Improvement for Battery Thermal Management System of a Hybrid Electric Aircraft- CFD Analysis, LTR-GTL-2023-0085, Ottawa: National Research Council Canada, Gas Turbine Laboratory, 2023.